CHARACTERISATION OF THE RADIAL VARIABILITY OF THE STIFFNESS PARAMETERS OF P. PINASTER BY THE VIRTUAL FIELDS METHOD

Xavier, J.[1], Avril S.[2], Pierron, F.[1], Morais, J.[3]

[1] LMPF/ENSAM, Chalons-en-Champagne, France
[2] ENSM, Saint-Etienne, France
[3] CITAB/UTAD, Vila Real, Portugal

ABSTRACT

In this work, the radial variability of longitudinal-radial stiffness parameters of maritime pine (P. pinaster) wood was investigated. The approach was based on the application of the virtual fields method (VFM) to a rectangular specimen loaded by the Iosipescu fixture. The displacement fields were measured by the grid method. The strain fields were then reconstructed from the measured displacement fields using a polynomial approximation scheme. Specimens with grain at 45º were tested. For this configuration, both the transverse (Q_{22}) and the shear (Q_{66}) stiffness parameters can be simultaneously identified. From the tested material, it was found that both these properties decrease from the centre to about the middle radius of the stem and increase afterwards at the outmost positions.

1- INTRODUCTION

The mechanical behaviour of wood can be quite complex owing to its biological nature. However, for low levels of stress (below the elastic limit), short periods of time (a few minutes) and minor variations of moisture content and temperature (absence of hygro-thermal environment effects), wood can be assumed as a linear elastic orthotropic material. Three directions of symmetry are defined by the geometry and arrangement of the wood cells: the longitudinal (*L*,1), the radial (*R*,2) and the tangential (*T*,3) directions. Besides, at the macroscopic scale (10-200 mm), clear wood (free from structural features such as knots or gross grain deviation) is usually modelled as a continuous and homogeneous material. In the *LR* plane of symmetry and under a state of plane stress, the constitutive linear elastic equation is completely defined by four stiffness parameters: Q_{11}, Q_{22}, Q_{12} and Q_{66}, or equivalently by four engineering constants: E_1, E_2, ν_{12} and G_{12} (see Eq. 4). These parameters are conventionally determined by carrying out several independent mechanical tests, from which a simple or a uniform strain state is assumed in the gauge region (statically determined tests) (Guitard, 1987).

The mechanical properties of wood vary within the stem of a tree, both radially and longitudinally. Nevertheless, experimental studies for accessing this spatial variability are limited, namely for properties perpendicular to the longitudinal direction. Machado and Cruz (2005) have studied the spatial variation of the longitudinal elastic modulus (E_1) of *P. pinaster* wood by standard bending tests. A huge amount of specimens were cut at different radial

positions and vertical locations, within and among trees. The authors have concluded that this modulus increase monotonically from the pitch to bark and slightly decrease with the high of the stem. However, to our best knowledge, no information about the spatial variability of other elastic parameters within the stem is available in the literature. This missing data can be justified by the fact that a great effort, from an experimental point of view, is required. On the one hand, due to wood anisotropy, various independent mechanical tests are usually required (*e.g.*, tensile, bending or shear tests). On the other hand, due to wood variability, a significant number of specimens need to be tested. Furthermore, in order to study the radial variation of the transverse stiffness (Q_{22}), standard macroscopic mechanical tests may not be suitable due to incompatibilities between specimen configuration and the cylindrical geometry of the stem.

The recent development of full-field optical techniques has enabled a new glance on the mechanical tests for material characterisation (Grédiac et al., 2006). The idea is to load a single specimen in such a way that several parameters are involved in the mechanical response, yielding heterogeneous and complex strain fields (statically undetermined tests). By means of a suitable identification strategy all the active parameters can eventually be determined afterwards. This approach has been already applied by the authors to *P. pinaster* wood, in order to find out a mechanical test allowing the identification of several *LR* stiffness parameters from a single specimen (Xavier et al., 2007). The proposed procedure was based on the application of the virtual fields method (VFM) to a rectangular specimen loaded by the Iosipescu fixture. The displacement fields were measured by the grid method. The strain fields were then reconstructed from the measured displacement fields using a global polynomial approximation scheme. It has been shown that both the Q_{22} and the Q_{66} parameters (transverse and shear stiffnesses) can be identified from a rectangular specimen with grain at 45º, with regard to the specimen longitudinal axis (Xavier et al., 2007). In this work this unnotched Iosipescu test was chosen for investigating the radial variability of both Q_{22} and Q_{66} stiffnesses within the stem.

2 – PARAMETER IDENTIFICATION FROM STATICALLY UNDETERMINED TEST

2.1 - Unnotched Iosipescu test

The mechanical test chosen in this work was the unnotched Iosipescu test (Figure 1). This test has been designed in such a way that a complex and inhomogeneous strain field is generated across the central part of the specimen. This mechanical response can be achieved by removing the V-notches from the classical geometry of the Iosipescu specimen, such that all the in-plane strain components can eventually contribute to the material deformation thanks to the shear/bending/compression stress distribution applied by the fixture. A $L \times W$ mm^2 gauge area was considered (Figure 1), because the magnitude of the strain gradients are expected to be more important in this region and the length to width ratio is not too enhanced with regard to the typical format of digital camera sensors.

In order to balance out the contribution of the different strain field components, and consequently enhance the identifiably of the in-plane constitutive parameters, an optimisation study was undertaken for calibrating the length between the inner supports (L) and the grain (fibre) angle (θ) (Xavier et al., 2007; Xavier, 2007). In this study, L = 34 mm and θ = 45º were chosen.

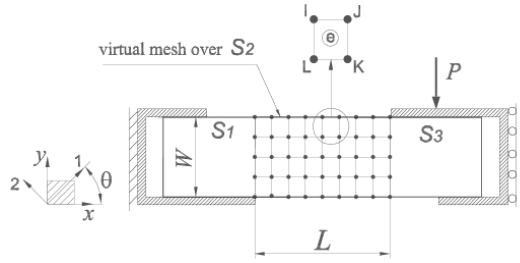

Fig 1 - Schematic of the unnotched Iosipescu test. *x-y* and *1-2* are the specimen and material coordinate systems, respectively

2.2 – Displacement measurement: Grid method

The grid method is a white-light optical technique which provides the measurement of the in-plane full-field displacements, by means of the analysis of the deformation of a grid. This grid consists of a periodic pattern of bright and dark lines. It is characterised by a spatial frequency vector **F** (orthogonal to the grid lines), has an amplitude equal to the inverse of the pitch of the grid (*p*) and its unit is lines/mm. From a single image of the grid, the phase (at each pixel) of the periodic function describing the grid pattern can be evaluated thorough a spatial phase-shifting method (Surrel, 1999). It can be demonstrate that the difference of phase ($\Delta\phi$) between the initial (undeformed) and the final (deformed) configurations is proportional to the imposed displacement field (*u*) by the following relationship (Surrel, 2004):

$$u_\beta(x,y) = -\frac{p}{2\pi}\Delta\phi_\beta(x,y) \qquad (1)$$

where $\beta =$ *x* or y, respectively for the horizontal (grid of vertical lines) or vertical (grid of horizontal lines) components of the displacement.

2.3 - Strain field reconstruction

The grid method provides the measurement of the displacement field, so an additional numerical denoising and differentiation procedure is needed to calculate the corresponding strain field, needed in the material characterisation problem. This was achieved by fitting a 2D polynomial function to the raw (unfiltered) displacement data using a least-squares approximation scheme:

$$\min_{\{a_\beta\}} \mathbf{w}\left(\mathbf{u}_\beta - \bar{\mathbf{u}}_\beta\right)^2 \quad \text{with}$$
$$\bar{\mathbf{u}}_\beta = \sum_{i,j}^{d} a_{\beta_{ij}} \mathbf{x}^i \mathbf{y}^j \quad (i+j<d) \qquad (2)$$

where **w** represents a weighting mask (binary image) defining the validity of each pixels, $a_{\beta ij}$ ($\beta =$ *x,y*) are the unknown polynomial coefficients, and *d* is the degree of the polynomial. The strain field can then be straightforwardly deduced by differentiating the polynomial displacement fields.

2.4 – Parameter identification: Virtual fields method

Let us consider a rectangular plate submitted to the unnotched Iosipescu test depicted in Figure 1. The problem to be solved is the simultaneous identification of the unknown elastic parameters involved in the material mechanical response. It is assumed that both the resultant applied load (P) – measured by the load cell of the testing machine – and the strain field across the surface of interest – *e.g.*, determined from the displacement field measured by the grid method – are known. Moreover, the specimen is assumed to be under a plane stress state.

The VFM is a suitable strategy for addressing this inverse parameter identification problem. It is based on the principle of virtual work (PVW). For the plane stress problem and in absence of body forces, the PVW can be written as (*i=1,2,6* and β*=x,y*):

$$\int_s \sigma_i \varepsilon_i^* dS = \frac{1}{t}\int_{s_f} T_\beta\left(M, n_\beta\right) u_\beta^*(M)\, dS \qquad (3)$$

where σ_i is the stress field, ε_i^* the virtual strain field, *S* the surface of interest of the plate, *t* the thickness of the plate, $T_\beta(M,n_\beta)$ the distribution of external tractions applied over S_f (*M* is any point of this surface and n_β the outward normal vector at point *M*) and u_β^* the virtual displacement field.

A constitutive model of the material must be assumed at this stage. Clear wood was modelled by the orthotropic linear elastic model, which can be written in the *LR (12*) plane of symmetry as:

$$\sigma_i = Q_{ij}\varepsilon_j \qquad (4a)$$

where the Q_{ij}'s are the material stiffness parameters:

$$Q_{ij} = \begin{bmatrix} Q_{11} & Q_{12} & 0 \\ Q_{21} & Q_{22} & 0 \\ 0 & 0 & Q_{66} \end{bmatrix} \quad (4b)$$

$$= \begin{bmatrix} \frac{E_1}{1-\upsilon_{12}\upsilon_{21}} & \frac{-\upsilon_{21}E_1}{1-\upsilon_{12}\upsilon_{21}} & 0 \\ \frac{-\upsilon_{12}E_2}{1-\upsilon_{12}\upsilon_{21}} & \frac{E_2}{1-\upsilon_{12}\upsilon_{21}} & 0 \\ 0 & 0 & G_{12} \end{bmatrix} \quad (4c)$$

Substituing the constitutive equation (Eq. 4) into the PVW (Eq. 3), and assuming a macroscopically homogenous material, a new equation can be obtained:

$$Q_{ij}\int_s \varepsilon_j \varepsilon_i^* dS = \frac{1}{t}\int_{s_f} T_\beta . u_\beta^* dS \quad (5)$$

involving the Q_{ij} unknown parameters, the ε_j actual strain components over S, the T_β applied tractions and the u_i^* and ε_i^* virtual fields. The above Eq. (5) is verified for any kinematically admissible (K.A.) virtual fields (u_i^*,ε_i^*), i.e., continuous and differentiable. At this stage, Eq. (5) is rewritten with, at least, as many independent K.A. virtual fields as there are unknown parameters. This procedure yields a linear system of equations in the form of:

$$[P]\{Q\} = \{R\} \quad (6)$$

Finally, this system of equations (Eq. 6) can be solved for the stiffness vector $\{Q\}$, providing that the virtual fields are selected so that $[P]$ can be inverted and that all the unknowns are involved in the mechanical response. The latter requirement is fulfilled when the strain field is heterogeneous and its components smoothly balanced across the gauge area. Because of the integral form of the PVW, this method is well adapted for processing full-field measurement obtained by a suitable optical method.

A key issue of the VFM is, however, the selection of the four virtual fields – among a large set of possibilities – since they directly affect the degree of independence of the equations in the system (6) and therefore the invertibility of matrix $[P]$. Although these virtual fields can be selected by hand in a trial-and-error approach, a general numerical procedure for their expression and selection was recently proposed (Grédiac et al., 2006). The advantage is that a large domain of search of the virtual fields can be explored, enhancing the robustness of the method. Moreover, expressions for the direct identification of the stiffness parameters can be obtained because the virtual fields can be built up such that matrix $[P]$, in Eqs. (6), is reduced to the identity matrix $[I]$. Such virtual fields, called special virtual fields ($\tilde{u}_\beta^*, \tilde{\varepsilon}_i^*$), can be expanded over a basis of functions (polynomials, for instance), either over the whole region of interest or in a piecewise manner as in the finite element method (Grédiac et al., 2006). A constrained optimisation scheme was proposed by (Avril et al., 2006) in order to select the special virtual fields that minimise the sensitivity of the VFM to noisy data (maximum likelihood solution). Such strategy was found to significantly improve the robustness of the method.

3 - EXPERIMENTAL WORK

3.1 - Wood material

The wood material used in this study was manufactured from a single *P. pinaster* tree, aged of 64 years and selected in the district of Viseu (Portugal). In order to study the radial distribution of the stiffness parameters, two groups of specimens were sampled along the radius of the stem at two distinct vertical locations, separated by about four meters, as schematised in Figure 2. For each vertical location in the stem, rectangular specimens with nominal dimensions 80(L) ×20(R)×5(T) mm^3 and grain at 45º, with respect to the specimen longitudinal axis, were cut along the radial direction from the pith to the outer part of the board (Figure 2). Because of some eccentricity and taper shape of the stem, the specimens were cut at four (r_1, r_2, r_3, r_4) and three (r_1, r_2, r_3) radial positions at the first (l_1) and second (l_2) vertical locations, respectively. For repeatability quantifica-

tion, at location 1, nine specimens per radial position were machined, *i.e.*, a total of thirty-six specimens; whereas, at location 2, eight specimens per radial position were prepared, *i.e.*, a total of twenty-four specimens. All specimens were free from visible defects and contained a few annual rings over the region of interest. The tests were carried out at a room temperature of 23.2±1.2ºC and at a relative humidity of 42.7±4.9%. After the tests, the specimens were dried and their moisture content during the tests was estimated, according to the oven-dry method, equal to 10.3±0.5%.

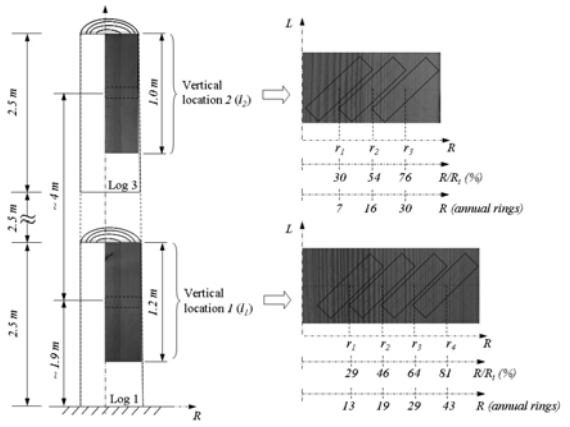

Fig 2 - Schematic representation of the specimen sampling within the stem

3.2 - Grid transfer

The pitch of the grid (p) was determined attending to the size of the region of interest (34(L) ×20(R) mm^2), the characteristics of the CCD sensor - resolution (1376(H) ×1040(V)) and size of the unit cells (6.45 μm) - and the number of pixels (N = 4) used for sampling a period of the grid. Accordingly, a pitch of 100 μm was chosen, corresponding to a spatial frequency of 10 lines/mm (low-frequency grating). In our experiments the grid was transferred according to the procedure proposed by (Piro and Grédiac, 2004). The first step consists in printing the network of crossed lines (*i.e.*, with horizontal and vertical superimposed orthogonal lines, with equal pitch in both directions) onto a photographic film (Ferrania photographic film AI PO-50®), made of a polymeric transparent support and a photosensitive emulsion coating. This film was then bonded onto the specimens as follows.

- After manufacturing, each specimen was polished using several grits of sandpaper (ranging from P240 up to P800). Particular care was given to the parallelism of the loading faces of the specimen and their perpendicularity to the front and back surfaces. The final dimensions of the specimens (length, width and thickness) as well as their grain orientation, were then determined as the mean value of at least three independent measurements. The gauge area at the centre of the specimens was delimited afterwards (Figure 3(a)). The gauge region was cleaned up using a cleaning agent (*e.g.*, acetone or alcohol) followed by M-Pre Neutralisant 5A (Vishey Measurement), as recommended in strain gauges bonding.
- From the photographic film (size A4) a piece with dimensions slightly higher than the gauge area was carefully cut and cleaned. This film was then placed over the region of interest of the specimen using a Sellotape bonded to one end. Special care must be taken to guarantee that the printed lines will be oriented with regard to the specimen edges.
- The film was bonded onto the specimen using the Epotechny E504® epoxy resin (Figure 3(b)). This glue has a white colour, which increases the final optical contrast of the grid pattern.
- A sufficient quantity of resin was poured at the base of the gauge region (figure 3(c)). While maintaining the film under an angle of about 30º, the glue was spread all over the extension of the gauge area by progressively laying the film, with low pressure and with the help of gauze. All spilt resin was removed afterwards.
- The grid (film+resin) was then covered with silicone rubber and subjected, during cure, to a small mass of about 50 g in order to create an even and thin layer with a thickness of about 0.1 mm.

The resin was then cured during a week at a constant temperature of 23ºC.

- After polymerisation of the resin, the back of the photographic film was carefully removed by pulling the film slowly and all in one go. Doing so, the coating of the film remains bonded to the glue defines a periodic bright and dark grating over the gauge area (Figure 3(d)).

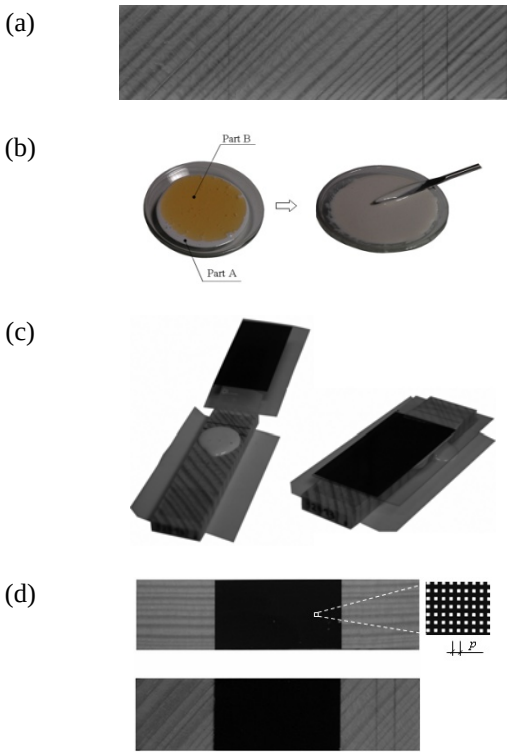

Fig 3 - Illustration of the steps in the grid transfer (p = 0.1 mm)

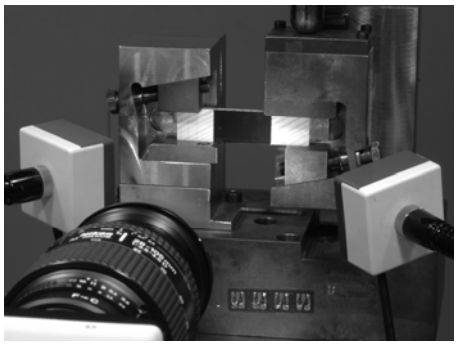

Fig 4 - Photomechanical set-up

3.3 - Measurement details

A PCO SenSicam CCD Camera connected to a PC, along with a Nikon AF Zoom–Nikkor 28–105mm f/3.5–4.5D IF lens and a 15 mm extension tube were used for image grabbing (Figure 4). The camera-lens system was mounted on a tripod and positioned in front of the specimen, with special attention paid to the alignment of the CCD sensor and grid planes. The image acquisition was performed with the software CamWare v2.03® supplied with the CCD camera. The focal length, the aperture of the lens and the exposure time, along with the working distance (defined as the distance between the object and the front of the camera) and light source intensity were carefully selected in order to achieve a grid image of good quality. In this context, this means a contrasted image of the grid lines (*i.e.*, with a histogram showing a relatively high ratio of maximum to minimum brightness, within the dynamic range of the camera sensor, over the region covered by the grid) and a magnification leading to approximately 4 pixels/period. More precisely, the calibration of the camera-lens optical system was performed as follows.

- After setting up the specimen into the fixture, the CCD camera was aligned with respect to the grid plane. Firstly, the camera is simply positioned in order that the imaged field of view will cover the whole gauge region (area delimited by the grid) throughout testing. Secondly, the spatial rotations of the camera are adjusted. A laser ruler can be used to achieve a correct parallelism between the camera sensor and grid planes. Moreover, with the grid method, the in-plane rotation (θ_Z) can be set using a moiré effect, providing that the sub-sampling image $I(x,y)/N$ (in our case N=4) can be monitored in real time. In such image, when the system parameters (*e.g.*, the focal length or the working distance) are adjusted so that each period of the grid is imaged by approximately N pixels, low-frequency crossed fringes (like in moiré) are visualised. Provided that some fringes are visible across the region of interest (*i.e.*, no perfect match of N pixels per period exists), they can be used to align the sensor array with respect to the grid lines. This is fulfilled

when parallel fringes, in both horizontal and vertical directions, are imaged.

- The magnification of the imaging system must be calibrated in order to fulfil the requirement of N pixels/period. The magnification (m) is determined as $m=p_{si}/p_{so}$, where p_{si} is the pixel size in the image plane whilst p_{so} is the pixel size in the object plane, determined in the grid method by $p_{si}=p/N$. In our experiments, m=6.45μm/25μm=0.258 (1:3.9). In practice, the adjustment of the magnification of the imaging system can be achieved in two ways. On the one hand, a scale can be fixed at the same plane as the grid; the calibration here consists in setting a given number of pixels over a known distance. On the other hand, the sub-sampling image (moiré effect described previously) can also be efficiently used for this purpose. In this case, the total number of fringes in the sub-sampling image ($I(x,y)/N$) must converge to zero. In the ideal situation, where no bias is introduced by an incorrect sampling, the moiré fringes in the image will completely lose their contrast. Experimentally, however, namely because of lens aberrations, only a close approximation is possible. In practice, the magnification can be controlled either by the working distance or by the focal length of the lens. In our experiments, the working distance was set to about 450 mm, and the focal length to 100 mm.
- The value of the exposure time was selected as a compromise between two conditions. On the one hand, throughout the exposure time, the specimen must not significantly move with regard to the CCD sensor, *i.e.*, the global rigid-body motion of the specimen (d) must remain small compared to the pixel size in the object plane (p_{so}). The time (t) fulfilling this condition can be evaluated from the kinematic expression: $t=d/v$, where v is the cross-head displacement rate of the testing machine. The exposure time can then be defined such that: $t<<p_{so}/v$. On the other hand, the integration time should be long enough to insure a high signal-to-noise ratio of the light signal magnitude compared to the measurement (intensity) uncertainty. Furthermore, the selection of this parameter is intrinsically related to the amount of light reflected by the specimen (which can be controlled by the aperture of the lens or directly by the potentiometer of the light source projected over the specimen), since both the duration and the intensity quantify the actual amount of light reaching the photosensitive areas (photodiods) of the camera and therefore the amount of electronic signal generated by the sensor. Therefore, as a compromise, an exposure time of 1/8=0.125 s (p_{so} = 25 μm, v = 1 mm/min) was chosen here.
- The image was carefully focused at the grid plane setting the lens aperture at f/2.3. For a given focal length and working distance, this maximum aperture (minimum f-number) corresponds to minimum depth of field (it represents the distance by which the object may be shifted back or forward still remaining in acceptable focus) in the image formation, which can be helpful in focusing exactly onto the plane of interest. However, before testing, the f-number was changed to a value of f/8 in order to improve the depth of field such that, throughout the test, even if the specimen is subjected to an out-of-plane motion (a few tenth of μm) the grid image will still remain in focus, *i.e.*, keeping its contrast.

The load and grid images were recorded automatically during the tests with an acquisition frequency of 2 Hz. From the sequence of grid images, the phase difference between each pair of consecutive measurements was evaluated. One advantage of this approach is that the computed change of phase between two consecutive acquisitions is not wrapped, *i.e.*, it is always obtained within the interval $[-\pi,\pi]$ because the undergoing displacements between two consecutive states does not exceed the pitch of the grid.

Therefore, the usual phase unwrapping process (Surrel, 1999) in data processing is avoided. For a given load level, the corresponding continuous displacement fields were subsequently determined by summing up the contributions of all previous incremental displacement fields.

In the grid method, the measurement of the in-plane displacement field is coupled to the out-of-plane motion of the specimen (ΔZ) because only one camera is used (monocular vision). If the specimen undergoes a given out-of-plane displacement during the test, the magnification of the optical system will be consequently changed (Δm). This induces a parasitic effect that is equivalent to an apparent uniform pitch variation. Hence, a non negligible apparent linear deformation of the grid can occur, being approximated by (thin-lens model): ε_β = Δm/m = - ΔZ/Z, where β = 1 or 2 for a grid with vertical or horizontal lines, respectively, and Z is the distance between the object and the lens centre. In our experiments, Z was around 350 mm, so if a strain resolution of 10^{-4} is targeted, it can be calculated that a ΔZ of about 35 μm can disturb the measurements. Therefore, in order to monitor the magnitude of ΔZ, a LVDT was placed on the back surface of the specimen during the experiments.

The spatial resolution of the grid method (*i.e.*, the smallest distance separating two independent measurements) is about the pitch of the grid, *i.e.*, 0.1 mm (gauge area of 34×20 mm^2). After the calibration of the optical system and before testing, the resolution (*i.e.*, the smallest value that can be detected or measured) associated to the phase measurements was globally evaluated by the standard deviation of the residual maps, resulting from the difference of phase fields of the same undeformed state of the grid/specimen. In practice, 7 images of the grid at rest were taken at intervals of 10 s and their phase evaluated. From the residual maps obtained by subtracting pairs of successive phase fields, a standard deviation vector was calculated (spatial uncorrelated measurements were assumed). The phase resolution (σ_θ) was then determined as the mean of the standard deviations. In our experiments, σ_θ was found to be about 3.05±0.5º. The displacement resolution (σ_u) was determined afterwards according to: $\sigma_u = \sigma_{\Delta\theta}/S$, where $S = 2\pi/p$ = 62.9 rad/mm. σ_u was determined in the range 1.20±0.2 μm. Moreover, it may be worth mentioning that the scatter of the resolution obtained here was strongly related to the quality of the grid transfer achieved in each specimen.

The tests were carried out using an Instron 5582 universal testing machine. The load was measured by a 5 kN load cell. It was applied at a constant cross-head displacement rate of 1 mm/min.

4 - RESULTS AND DISCUSSION

The stiffness parameters were identified by the virtual fields method (VFM), processing the displacement fields measured experimentally by the grid method. These raw displacement fields were filtered by a 7th-degree polynomial using the least-squares regression scheme. The strain fields were then determined by finite differences from the polynomial displacement fields. Piecewise optimised virtual fields were defined over a mesh of 5(x)×3(y) elements. Both the computed strain fields and the applied load, corresponding to different acquisition times, were input into the VFM routine for the identification of the stiffness parameters. For filtering purposes, the parameters were determined as the mean of a set of identified values obtained within a specified range of loads. In order to select this range of loads, a parameter identification was performed between 100N and 300N. If the results have a coefficient of variation larger than 10%, then the data, corresponding to the identified stiffness values that are higher than ±2σ about the mean, are systematically removed in further revaluations until convergence is eventually reached.

As somewhat expected from previous results (Xavier et al. 2007), the identification of both Q_{11} and Q_{12} was too scattered. Therefore, only the results for Q_{22} and Q_{66} are reported thereafter.

The identification results are shown in Figure 5(a) and (b) for Q_{22} and Q_{66}, respectively, as a function of the radial position at the two vertical locations. As it can be seen, a contrast can be observed between values identified at different radial positions. As a general pattern, both Q_{22} and Q_{66} decrease from the inner position to about the middle radius of the stem and increase afterwards to the outermost positions. Besides, the radial variability of Q_{22} is higher than the one obtained for Q_{66}, *i.e.*, with a contrast ranging between 49%-72% and 18%-27% (depending on the location within the stem), respectively. The variation of the oven-dry density of the specimens (determined as the ratio between the oven-dry weight and green volume) along the radial direction did not explain by itself the pattern of the stiffness spatial distribution (Figure 6). This supports the point that other structural features (*e.g.*, geometry of the wood cells, percentage of juvenile and mature wood of the specimens, microfibril angle...) are to be considered in order to understand the origin of the radial variation of the elastic properties. This issue is under further investigation.

(a)

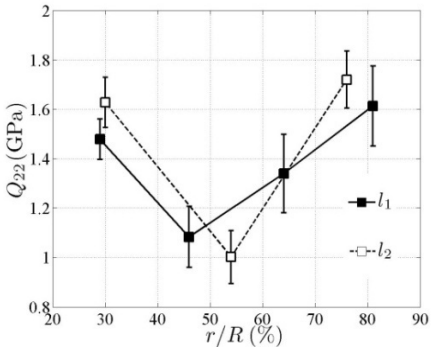

(b)

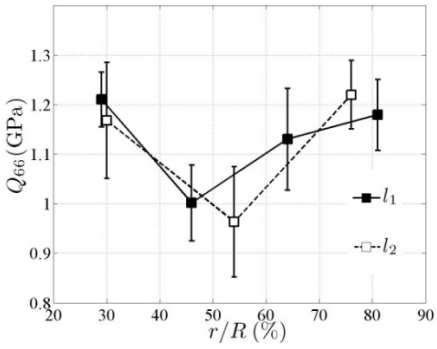

Fig 5 - Variation of the stiffness parameters: (a) Q_{22}, (b) Q_{66}, identified at the two vertical locations 1 (■) and 2 (□) as a function of the radial position (r/R)

5 - CONCLUSIONS

In this work, the radial spatial variability of longitudinal-radial, (L,R≡1,2), stiffness parameters of clear wood of *P. pinaster* within the stem was investigated. Small unnotched specimens with grain at 45º were sampled at different radial locations within the stem and tested using the Iosipescu fixture. For this configuration both the transverse (Q_{22}) and the shear (Q_{66}) stiffness parameters can be simultaneously determined. The virtual fields method (VFM) was used to extract the stiffness parameters from the displacement fields measured by the grid method. The following main conclusions were drawn.

- It was found that along the radial direction both the Q_{22} and the Q_{66} parameters decrease from the innermost position to about the middle radius of the stem and increase afterwards to the outermost positions. Besides, the radial spatial variability of Q_{22} was found higher than the one obtained for Q_{66}, *i.e.*, with a contrast ranging between 49%-72% and 18%-27% (depending on the location within the stem), respectively.

(a)

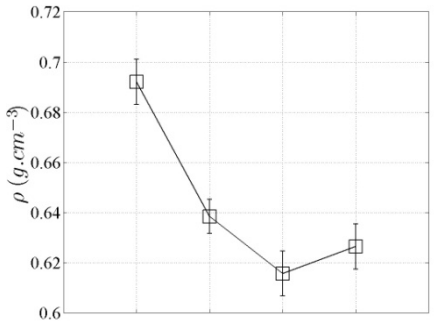

(b)

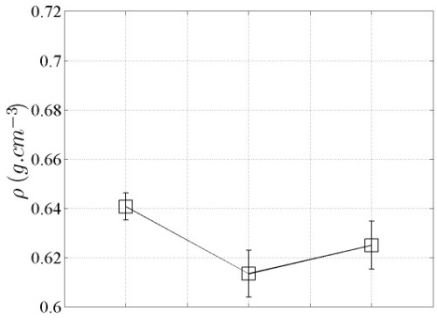

Fig 6 - Variation of the density identified at the two vertical locations 1 (a) and 2 (b) as a function of the radial position (r/R)

- No significant longitudinal variation was observed for both Q_{22} and Q_{66} parameters within the two studied vertical locations. However, the data provided here may not be sufficient to supply a relevant pattern of the longitudinal variations of the stiffness parameters.
- The density variation of the specimens along the radial direction did not explain by itself the pattern of the stiffness variation. This supports the point that other structural features (*e.g.*, microfibril angle, percentage of juvenile and mature wood of the specimens...) are to be considered in order to understand the origin of the radial variation of the elastic properties.

The results from this work can be used as indicative values in a further study, aiming at identifying the radial variability of several elastic parameters directly from a single specimen. The idea is to carry out a bending test over a plate taken from the pith to the bark of the stem. The radial variability of the stiffness parameters can be parameterised using a polynomial basis function, for instance. A similar procedure of the VFM has already been developed for the identification of the local stiffness reduction on damaged composite plates (Kim et al., 2007).

ACKNOWLEDGEMENTS

We would like to thank João Luís Pereira and Marcelo Oliveira for their help in the wood material preparation and the Foundation for Science and Technology (FCT) for the Ph.D. scholarship of J. Xavier.

REFERENCES

Grédiac, M., Pierron, F., Avril, S., and Toussaint, E., The virtual fields method for extracting constitutive parameters from full-field measurements: a review, Strain, 42(4):233–253, 2006

Guitard, D., Méchanique du matériau bois et composites, Cepadues-Editions, Collection Nabla, 1987

Machado, J.S. and Cruz, H.P., Within stem variation of Maritime Pine timber mechanical properties, Holz als Roh - und Werkstoff, 63(2):154–159, 2005

Surrel, Y., Fringe analysis, In P.K. Rastogi, editor, Photomechanics (Topics in Applied Physics), pages 57–104. Springer Verlag, 1999

Surrel, Y., La technique de la grille pour la mesure de champs de déplacements et ses applications, Instrumentation, Mesure, M,trologie, 4(3-4):193–216, 20

Xavier, J., Avril, S., Pierron, F., Morais, J., Novel experimental approach for longitudinal-radial stiffness characterisation of clear wood by a single test, Holzforschung 61(5): 573-581, 2007

Xavier, J., Characterisation of the wood stiffness variability within the stem by the virtual fields method: application to P. pinaster in the LR plane, Ph.D. Thesis, ENSAM Châlons-en-Champagne, France, 2007

Avril, S., Grédiac, M., Pierron, F., Sensitivity of the virtual fields method to noisy data, Computational Mechanics, 34(6):439-452, 2004

Piro, J.-L., Grédiac, M., Producing and transferring low-spatial-frequency grids for measuring displacement fields with moiré and grid methods, Experimental Techniques, 28(4):23-26, 2004

Kim, J.-H., Pierron, F., Wisnom, M.R., Syed-Muhamad, K.. Identification of the local stiffness reduction of a damaged composite plate using the virtual fields method, Composites Part A: Applied Science and Manufacturing,38(9):2065-2075,2007